Pinning-depinning of the contact line during drop evaporation on textured surfaces: A lattice Boltzmann study

Kamal Jannati, Mohammad Hassan Rahimian,* and Mostafa Moradi
School of Mechanical Engineering, College of Engineering, University of Tehran, Tehran, Iran

(Received 3 May 2020; revised 20 July 2020; accepted 14 August 2020; published 9 September 2020)

The evaporation of the liquid droplet on a structured surface is numerically investigated using the lattice Boltzmann method. Simulations are carried out for different contact angles and pillar widths. From the simulation for the Cassie state, it is found that the evaporation starts in a pinned contact line mode. Then, when the droplet reaches the receding state, the contact line jumps to the neighboring pillar. Also, the depinning force decreases with increasing the contact angle or the pillar width. In the Wenzel state, the droplet contact line remains on the initial pillar for all of its lifetime.

DOI: 10.1103/PhysRevE.102.033106

I. INTRODUCTION

Evaporation of the liquid droplets is an important fundamental topic in a wide range of applications, such as surface patterning [1], biosensing [2], inkjet printing [3], DNA mapping [4], and droplet-based microfluidics [5]. All of these applications involve microscale droplets. At such small scales, surface phenomena are the dominant factors and the dynamics of droplets are governed by inertial-capillary forces, rather than the action of gravity [6]. The study of the already complex droplet evaporation process becomes even more challenging in the presence of solid substrates. It has been shown that the dynamics of sessile droplet evaporation is directly linked to substrate characteristics, such as surface wettability [7], contact angle hysteresis [8], and surface roughness [9]. Understanding the evaporation characteristics of sessile droplets plays an invaluable role in the field of surface engineering and development of synthetic low-adhesion surfaces.

Roughness is a key parameter on textured surfaces [10]. The presence of surface structures on nano- and microcales alters the dynamics of droplets during evaporation. Picknett and Bexon [11] suggested two different modes of evaporation for sessile droplets: (1) constant contact radius (CCR) mode, in which the contact angle decreases with time and the contact area is fixed; (2) constant contact angle (CCA) mode, in which the contact angle is fixed and the contact area decreases during evaporation.

During droplet evaporation on textured surfaces, due to the pinning of the triple line (the liquid-vapor-solid line), a stick-slip (SS) pattern starts to emerge. Usually, there is one or several sticky state(s) in which the contact line is pinned (CCR mode), and one or several slippery state(s) in which the contact line is depinned (CCA mode) [12]. McHale *et al.* [6] experimentally showed that on superhydrophobic surfaces, the evaporation starts at the CCR mode and then a transition to the SS mode takes place. In some cases, when the droplet was initially in the Cassie state, they reported a collapse into the pillars during evaporation, where the liquid penetrates into the interpillar cavities. For the collapsed droplets, evaporation continues in the CCR mode.

By microscopic and macroscopic observations, Chen *et al.* [13] showed that the contact line dynamics has a strong dependence on pillar structure. They developed a model that can predict the depinning onset time and critical base size for the collapsing droplets. Dash and Garimella [14] investigated the evaporation of the water droplet on hydrophobic and superhydrophobic surfaces. Their results showed that the rate of evaporation is 20% smaller than the rate predicted by the vapor-diffusion-based model for superhydrophobic surfaces.

Xu and Choi [15] explored the effects of the patterned surface on the contact line and its pinning-depinning behavior for an evaporating droplet. For determining the depinning force, their results showed that a liquid-solid contact area and an apparent contact line is not a critical parameter. Choi and Kim [16] explored the evaporation process on a nanostructured surface for water droplets and a protein solution. They reported a different evaporation process for a water droplet and protein solution.

Popov [17] proposed a model for evaporating sessile drops on a horizontal flat surface. He found that the elapsed time from the start of the evaporation process, the initial concentration of the solute, and the initial geometry are the variables that determine the geometrical aspects of the deposition patterns. The model was solved analytically and numerically. The results were in good agreement with the experimental data.

Vapor-diffusion-based evaporation models have been widely employed to predict the droplet evaporation characteristics [8,12,17–22]. In these models, systems are assumed to be at a constant temperature. The natural result of this assumption is neglecting the evaporation rate due to the temperature gradient at the interface.

The lattice Boltzmann method has become a popular tool for simulating multiphase flow systems in recent decades. The original multiphase models in the LBM framework are limited

*rahimyan@ut.ac.ir

to low density and viscosity ratios and suffer from parasitic currents [23]. These purely numerical currents, which are caused by minor imbalances in the fluid-fluid interface, limit the range of parameters that can be achieved in the numerical model. Lee and Fischer [24], with the use of the potential form of the intermolecular force and compact isotropic difference of the forcing term, presented a method for simulating two-phase flow in the LBM framework that overcomes these limitations. In their model, parasitic currents could be reduced to the machine accuracy while the density ratio is up to 1000. Later on, Safari *et al.* [25] extended this model for simulation of thermal phase change in two-phase fluid flows.

The objective of this work is performing a lattice Boltzmann simulation to explore the effects of surface topology and contact angle on the dynamics of the drop contact line during evaporation caused by the temperature gradient at the interface. The LBM is implemented with the use of the model of Safari *et al.* that is capable of modeling thermal phase change at high density and viscosity ratios.

In the rest of the paper, the following sections will be presented. In Sec. II, the governing equations, including the Cahn-Hilliard in the presence of phase change, hydrodynamic, and energy equations are presented. Numerical validation and results are presented in Secs. III and IV, respectively. Finally, the paper is concluded in Sec. V.

II. GOVERNING EQUATIONS

A. Extension of Cahn-Hilliard equation

The continuity equation for a system of two incompressible and immiscible fluids, with different bulk density and viscosity, can be written as

$$\frac{\partial \tilde{\rho}_i}{\partial t} + \nabla \cdot \boldsymbol{n_i} = \stackrel{+}{-}\dot{m}''', \tag{1}$$

where $\tilde{\rho}_i$ is the bulk density and $\boldsymbol{n_i}$ is the mass flow rate of the species i (l for the liquid phase and g for the gas phase), and $\stackrel{+}{-}\dot{m}'''$ is the volumetric source due to phase change. The mass flow rate of component i can be written as

$$\boldsymbol{n_i} = \boldsymbol{u}\tilde{\rho}_i - \rho_i \boldsymbol{j}_i. \tag{2}$$

The first term in the above equation is due to the advection in the bulk region and the second term is due to the diffusive mass flow in the interfacial region. $\boldsymbol{u}$ is the velocity, $\boldsymbol{j}$ is the volume diffusive flow rate, and ρ is the local density.

The continuity equation in terms of the phase composition can be written as

$$\frac{\partial C}{\partial t} + \nabla \cdot (\boldsymbol{u}C) - \nabla \cdot \boldsymbol{j_l} = -\frac{\dot{m}'''}{\rho_l}, \tag{3}$$

$$\frac{\partial (1-C)}{\partial t} + \nabla \cdot [\boldsymbol{u}(1-C)] - \nabla \cdot \boldsymbol{j_g} = -\frac{\dot{m}'''}{\rho_g}, \tag{4}$$

where

$$\tilde{\rho}_l = C\rho_l, \tag{5}$$

$$\tilde{\rho}_g = (1-C)\rho_g, \tag{6}$$

and

$$\rho = C\rho_l + (1-C)\rho_g. \tag{7}$$

The composition C takes a value 1 in the liquid phase and 0 in the gas phase.

If the diffusive flow rate is only related to phase compositions, then $\boldsymbol{j_l} = -\boldsymbol{j_g} = \boldsymbol{j}$. Thus, from Eqs. (3) and (4) the divergence of the velocity field can be written as

$$\nabla \cdot \boldsymbol{u} = \dot{m}'''\left(\frac{1}{\rho_g} - \frac{1}{\rho_l}\right). \tag{8}$$

Cahn and Hilliard assumed that the diffusive flow rate is proportional to the gradient of the chemical potential:

$$\boldsymbol{j} = -M\nabla\mu, \tag{9}$$

where M is the mobility of the Cahn-Hilliard equation. According to [26], the chemical potential for binary fluids is

$$\mu = \beta(2C - 6C^2 + 4C^3) - \kappa\nabla^2 C, \tag{10}$$

where β and κ related to the surface tension σ by $\kappa = 1.5\sigma D$ and $\beta = 12\sigma/D$. D is the interface thickness.

Finally, the transport equation that governs the behavior of the binary-fluids system is

$$\frac{\partial C}{\partial t} + \nabla \cdot (\boldsymbol{u}C) = \nabla \cdot (M\nabla\mu) - \frac{\dot{m}'''}{\rho_l}. \tag{11}$$

The volumetric mass source of evaporation can be obtained by applying the energy balance on the interface. After some mathematical operations, volumetric mass source is

$$\dot{m}''' = \frac{K\nabla T}{h_{fg}} \cdot \nabla C, \tag{12}$$

where K is the thermal conductivity, h_{fg} is the latent heat of vaporization, and T is the temperature. More details can be found in [25].

B. LBE for hydrodynamics

In this paper, the method that was proposed in [24], based on the Lee method, is used for simulating the flow field. The discrete Boltzmann equation (DBE) with intermolecular interaction force can be written as

$$\begin{aligned}\frac{Df_\alpha}{Dt} &= \frac{\partial f_\alpha}{\partial t} + \boldsymbol{e}_\alpha \cdot \nabla f_\alpha \\ &= -\frac{1}{\lambda}\left(f_\alpha - f_\alpha^{\mathrm{eq}}\right) + \frac{1}{\rho c_s^2}(\boldsymbol{e}_\alpha - \boldsymbol{u}) \cdot \boldsymbol{F} f_\alpha^{\mathrm{eq}}.\end{aligned} \tag{13}$$

In the above equation, f_α is the particle distribution function, λ is the relaxation time, f_α^{eq} is the equilibrium distribution function, $\boldsymbol{e}_\alpha$ is the microscopic lattice velocity, c_s^2 is the sound speed, and $\boldsymbol{F}$ is the intermolecular interaction force.

Equilibrium distribution function f_α^{eq} is

$$f_\alpha^{\mathrm{eq}} = \omega_\alpha \rho\left[1 + \frac{\boldsymbol{e}_\alpha \cdot \boldsymbol{u}}{c_s^2} + \frac{(\boldsymbol{e}_\alpha \cdot \boldsymbol{u})^2}{2c_s^4} - \frac{(\boldsymbol{u} \cdot \boldsymbol{u})}{2c_s^2}\right]. \tag{14}$$

ω_α is the weight factor of the D2Q9 lattice structure. The intermolecular interaction force for binary fluids, that is presented by [24] is

$$\boldsymbol{F} = \nabla \rho c_s^2 - \nabla p_h - C\nabla\mu, \tag{15}$$

where p_h is the hydrodynamic pressure.

By introducing a new distribution function as follows, the DBE for the hydrodynamic pressure can evolve pressure instead of density:

$$g_\alpha = f_\alpha c_s^2 + \left(p_h - \rho c_s^2\right)\Gamma_\alpha(0), \tag{16}$$

where $\Gamma_\alpha(\boldsymbol{u}) = f_\alpha^{\mathrm{eq}}/\rho$. By taking the total derivative of Eq. (15), the DBE for the new distribution function becomes

$$\frac{Dg_\alpha}{Dt} = c_s^2\frac{Df_\alpha}{Dt} + \left(\frac{Dp_h}{Dt} - c_s^2\frac{D\rho}{Dt}\right)\Gamma_\alpha(0). \tag{17}$$

By assuming that the phase change has no effect on the incompressibility of two phases and does not affect the hydrodynamic pressure, the total derivative of hydrodynamic pressure and density becomes [25]

$$\frac{D\rho}{Dt} = (\boldsymbol{e}_\alpha - \boldsymbol{u})\cdot\nabla\rho - \dot{m}'''\rho\left(\frac{1}{\rho_g} - \frac{1}{\rho_l}\right), \tag{18}$$

$$\frac{Dp_h}{Dt} = (\boldsymbol{e}_\alpha - \boldsymbol{u})\cdot\nabla p_h. \tag{19}$$

By substituting these derivatives into Eq. (17), the DBE for the hydrodynamic pressure and momentum is as follows:

$$\frac{\partial g_\alpha}{\partial t} + \boldsymbol{e}_\alpha\cdot\nabla g_\alpha = -\frac{1}{\lambda}\left(g_\alpha - g_\alpha^{\mathrm{eq}}\right) + (\boldsymbol{e}_\alpha - \boldsymbol{u})\cdot\left\{\nabla\rho c_s^2[\Gamma_\alpha - \Gamma_\alpha(0)] - C\nabla\mu\Gamma_\alpha\right\} + \rho c_s^2\dot{m}'''\rho\left(\frac{1}{\rho_g} - \frac{1}{\rho_l}\right)\Gamma_\alpha(0), \tag{20}$$

and the new equilibrium distribution function is

$$g_\alpha^{\mathrm{eq}} = \omega_\alpha\left\{p_h + \rho c_s^2\left[\frac{\boldsymbol{e}_\alpha\cdot\boldsymbol{u}}{c_s^2} + \frac{(\boldsymbol{e}_\alpha\cdot\boldsymbol{u})^2}{2c_s^4} - \frac{(\boldsymbol{u}\cdot\boldsymbol{u})}{2c_s^2}\right]\right\}. \tag{21}$$

By applying the trapezoidal rule over time step δt, the LBE of Eq. (20) can be derived as

$$\begin{aligned}\bar{g}_\alpha(\mathbf{x} + \boldsymbol{e}_\alpha\delta t, t + \delta t) - \bar{g}_\alpha(\mathbf{x}, t) = &-\frac{1}{\tau + 0.5}\left(\bar{g}_\alpha - \bar{g}_\alpha^{\mathrm{eq}}\right)\Big|_{(\mathbf{x},t)} + \delta t(\boldsymbol{e}_\alpha - \boldsymbol{u})\cdot\left\{\nabla\rho c_s^2[\Gamma_\alpha - \Gamma_\alpha(0)] - C\nabla\mu\Gamma_\alpha\right\}_{(\mathbf{x},t)} \\ &+ \frac{\delta t}{2}\rho c_s^2\dot{m}'''\rho\left(\frac{1}{\rho_g} - \frac{1}{\rho_l}\right)\Gamma_\alpha(0)\Big|_{(\mathbf{x},t)} + \frac{\delta t}{2}\rho c_s^2\dot{m}'''\rho\left(\frac{1}{\rho_g} - \frac{1}{\rho_l}\right)\Gamma_\alpha(0)\Big|_{(\mathbf{x}+\boldsymbol{e}_\alpha\delta t, t+\delta t)},\end{aligned} \tag{22}$$

where τ is related to the kinematic viscosity by $\upsilon = \tau c_s^2$. $\bar{g}_\alpha$ and $\bar{g}_\alpha^{\mathrm{eq}}$ are defined to retain the scheme explicit.

$$\bar{g}_\alpha = g_\alpha + \frac{\left(g_\alpha - g_\alpha^{\mathrm{eq}}\right)}{2\tau} - \frac{\delta t}{2}(\boldsymbol{e}_\alpha - \boldsymbol{u})\cdot\left\{\nabla\rho c_s^2[\Gamma_\alpha - \Gamma_\alpha(0)] - C\nabla\mu\Gamma_\alpha\right\}, \tag{23}$$

$$\bar{g}_\alpha^{\mathrm{eq}} = g_\alpha^{\mathrm{eq}} - \frac{\delta t}{2}(\boldsymbol{e}_\alpha - \boldsymbol{u})\cdot\left\{\nabla\rho c_s^2[\Gamma_\alpha - \Gamma_\alpha(0)] - C\nabla\mu\Gamma_\alpha\right\}. \tag{24}$$

Hydrodynamic variables can be calculated by the first and second moment of the distribution function.

$$\rho\boldsymbol{u} = \frac{1}{c_s^2}\sum_\alpha \boldsymbol{e}_\alpha\bar{g}_\alpha - \frac{\delta t}{2}C\nabla\mu, \tag{25}$$

$$p_h = \sum_\alpha \bar{g}_\alpha + \frac{\delta t}{2}\boldsymbol{u}\cdot\nabla\rho c_s^2. \tag{26}$$

C. LBE for interface tracking

A new distribution function should be considered for calculating the composition. This distribution function should recover the extended Cahn-Hilliard equation for phase change phenomenon. It is convenient to choose this distribution function to have a simple form of $h_\alpha = (C/\rho)f_\alpha$ and $h_\alpha^{\mathrm{eq}} = (C/\rho)f_\alpha^{\mathrm{eq}}$; then the DBE can be derived by taking the total derivative of this expression. The total derivative of the composition from [25] can be written as

$$\frac{DC}{Dt} = (\boldsymbol{e}_\alpha - \boldsymbol{u})\cdot\nabla C - C\nabla\cdot\boldsymbol{u} + \nabla\cdot(M\nabla\mu) - \frac{\dot{m}'''}{\rho}. \tag{27}$$

Then the DBE for h can be written as

$$\frac{\partial h_\alpha}{\partial t} + \boldsymbol{e}_\alpha\cdot\nabla h_\alpha = -\frac{1}{\lambda}\left(h_\alpha - h_\alpha^{\mathrm{eq}}\right) + (\boldsymbol{e}_\alpha - \boldsymbol{u})\cdot\left[\nabla C - \frac{C}{\rho c_s^2}(\nabla p_h + C\nabla\mu)\right]\Gamma_\alpha + \left(M\nabla^2\mu - \frac{\dot{m}'''}{\rho_l}\right)\Gamma_\alpha \tag{28}$$

By applying a trapezoidal rule over time step δt, the LBE can be written as

$$\begin{aligned}\bar{h}_\alpha(\mathbf{x} + \boldsymbol{e}_\alpha\delta t, t + \delta t) - \bar{h}_\alpha(\mathbf{x}, t) = &-\frac{1}{\tau + 0.5}\left(\bar{h}_\alpha - \bar{h}_\alpha^{\mathrm{eq}}\right)\Big|_{(\mathbf{x},t)} + \delta t(\boldsymbol{e}_\alpha - \boldsymbol{u})\cdot\left[\nabla C - \frac{C}{\rho c_s^2}(\nabla p_h + C\nabla\mu)\right]\Gamma_\alpha\Big|_{(\mathbf{x},t)} \\ &+ \frac{\delta t}{2}\left(M\nabla^2\mu - \frac{\dot{m}'''}{\rho_l}\right)\Gamma_\alpha\Big|_{(\mathbf{x},t)} + \frac{\delta t}{2}\left(M\nabla^2\mu - \frac{\dot{m}'''}{\rho_l}\right)\Gamma_\alpha\Big|_{(\mathbf{x}+\boldsymbol{e}_\alpha\delta t, t+\delta t)}\end{aligned} \tag{29}$$

where $\bar{h}_\alpha$ and $\bar{h}_\alpha^{\rm eq}$ are

$$\bar{h}_\alpha = h_\alpha + \frac{\left(h_\alpha - h_\alpha^{\rm eq}\right)}{2\tau} - \frac{\delta t}{2}(\boldsymbol{e}_\alpha - \boldsymbol{u}) \cdot \left[\nabla C - \frac{C}{\rho c_s^2}(\nabla p_h + C\nabla\mu)\right]\Gamma_\alpha, \tag{30}$$

$$\bar{h}_\alpha^{\rm eq} = h_\alpha^{\rm eq} - \frac{\delta t}{2}(\boldsymbol{e}_\alpha - \boldsymbol{u}) \cdot \left[\nabla C - \frac{C}{\rho c_s^2}(\nabla p_h + C\nabla\mu)\right]\Gamma_\alpha. \tag{31}$$

For avoiding implicitness in the scheme, the last terms in Eqs. (22) and (29) are approximated at $\mathbf{x} + \boldsymbol{e}_\alpha \delta t, t$ and according to [25], this approximation does not disturb the second-order accuracy of the equations.

The composition is equal to the zero-order moment of the distribution function.

$$C = \sum_\alpha \bar{h}_\alpha. \tag{32}$$

The relaxation time of the phases is calculated as follows:

$$\tau = C\tau_l + (1 - C)\tau_g, \tag{33}$$

where τ_l and τ_g are the relaxion times of liquid and gas, respectively.

D. LBE for temperature field

Because of the low Mach number (Ma) and the incompressible flow assumption, in the hydrodynamic simulation, we can neglect the effects of the pressure work and heat dissipation in evaluating the temperature field. With this assumption, a simple passive convection-diffusion equation can be solved for temperature in the LB framework and temperature advected in the domain with macroscopic velocity $\boldsymbol{u}$. The DBE for the temperature convection-diffusion equation can be written as

$$\frac{\partial s_\alpha}{\partial t} + \boldsymbol{e}_\alpha \cdot \nabla s_\alpha = -\frac{1}{\lambda_T}\left(s_\alpha - s_\alpha^{\rm eq}\right), \tag{34}$$

and the equilibrium distribution function is

$$s_\alpha^{\rm eq} = \omega_\alpha T\left[1 + \frac{\boldsymbol{e}_\alpha \cdot \boldsymbol{u}}{c_s^2}\right]. \tag{35}$$

Again, by applying the trapezoidal rule over time step δt, the LBE can be derived as follows:

$$s_\alpha(\mathbf{x} + \boldsymbol{e}_\alpha \delta t, t + \delta t) - s_\alpha(\mathbf{x}, t) = -\frac{\left(s_\alpha - s_\alpha^{\rm eq}\right)}{2\tau_T}\bigg|_{(\mathbf{x}+\boldsymbol{e}_\alpha\delta t, t+\delta t)} - \frac{\left(s_\alpha - s_\alpha^{\rm eq}\right)}{2\tau_T}\bigg|_{(\mathbf{x},t)}. \tag{36}$$

In Eq. (36) τ_T is the nondimensional relaxation time that relates to the thermal diffusion coefficient by $\alpha = c_s^2 \tau_T \delta t$. To maintain the scheme explicit, the modified distribution function is introduced as follows:

$$\bar{s}_\alpha(\mathbf{x}, t) = s_\alpha(\mathbf{x}, t) + \frac{\left(s_\alpha - s_\alpha^{\rm eq}\right)}{2\tau_T}. \tag{37}$$

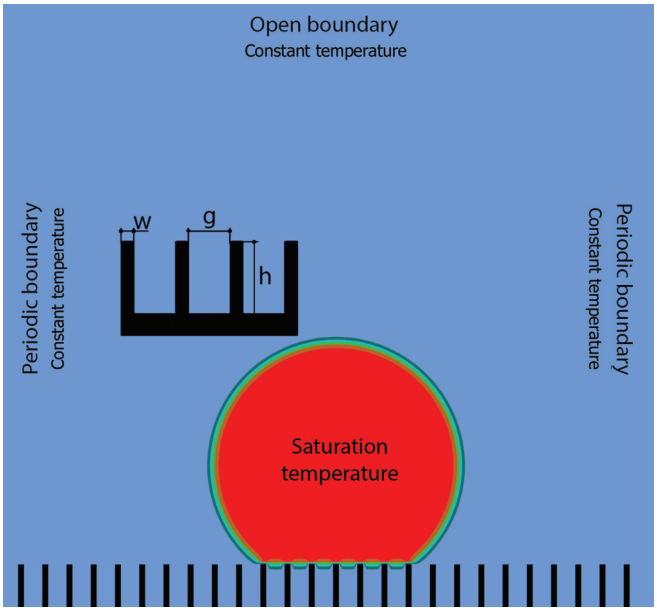

FIG. 1. Boundary conditions and pillar properties.

Then the LBE for the modified distribution function becomes

$$\bar{s}_\alpha(\mathbf{x} + \boldsymbol{e}_\alpha \delta t, t + \delta t) - \bar{s}_\alpha(\mathbf{x}, t) = -\frac{\left(\bar{s}_\alpha - \bar{s}_\alpha^{\rm eq}\right)}{\tau_T + 0.5}\bigg|_{(\mathbf{x},t)}. \tag{38}$$

Temperature can be calculated by taking the zero-order moment of the distribution function.

$$T = \sum_\alpha \bar{s}_\alpha. \tag{39}$$

It should be noted that this LBE for the temperature convection-diffusion equation recovers the unwanted term at the macroscopic level in the form $\frac{\alpha}{c_s^2}\frac{\partial}{\partial t}\nabla \cdot (\boldsymbol{u}T)$. According to [25], this term is of the order Ma^2 and can be neglected.

E. Boundary conditions

In this work, bounce back on the node scheme is applied on the solid boundaries. The upper boundary is considered to be an open boundary in the form of $\frac{\partial p_h}{\partial n} = 0$. Left and right boundaries are considered to be periodic. On the solid boundaries, $\boldsymbol{n} \cdot \nabla\mu|_s = 0$ is applied to ensure no mass flux normal to the boundaries. To impose a specific equilibrium contact angle, the cubic boundary condition is used:

$$\boldsymbol{n} \cdot \nabla C|_s = -\cos\theta\sqrt{\frac{2\beta}{\kappa}}\left(C_s - C_s^2\right), \tag{40}$$

where θ is the contact angle. Details of the implementation of these boundary conditions (B.C.) on the pillars for distribution functions and macroscopic variables can be found in [26]. A constant temperature, T_g, is imposed on the boundaries as the B.C. for the temperature field. Also, during evaporation the temperature of the droplet is set equal to the saturation temperature T_s by Eq. (35). See Fig. 1.

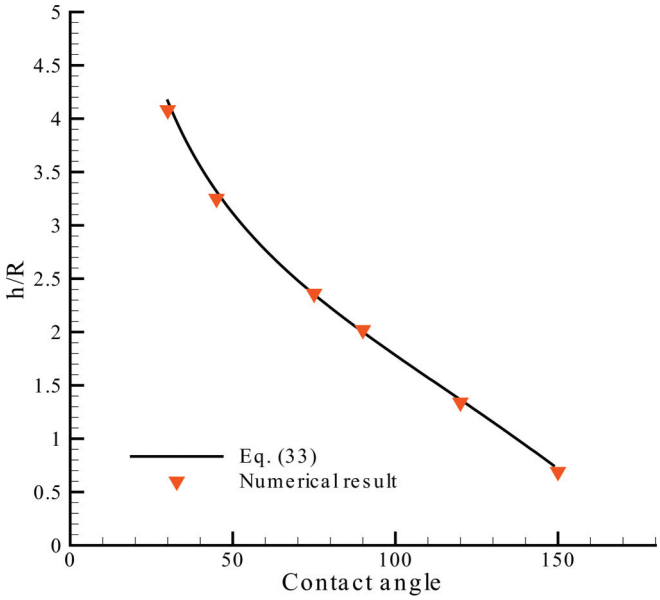

FIG. 2. Variation of the droplet height with contact angle. Solid line is given by Eq. (41) and triangular symbol shows the numerical result.

III. NUMERICAL VALIDATION

Validation of the numerical scheme is presented here. The first two tests validate the hydrodynamic behavior of the droplet, and the third one is to validate the evaporation of the droplet.

A. Contact angle on a flat surface

First test for validation of the numerical codeis simulating the wetting phenomenon on the flat surface. Different static contact angles are successfully achieved by setting the desired contact angle in Eq. (40). In the simulation no body force is applied to the phases, and a droplet with $R = 35$ lattice unit (lu) is initially placed on the bottom surface in a $5R \times 4R$ computational domain. These parameters are fixed in the simulation: $\rho_l = 1$, $\rho_g = 0.1$, $\tau_l = 0.5$, $\tau_g = 0.5$, $\sigma = 0.005$, and $D = 4$ lu. The numerical contact angle measured by calculating the slope of the composition contour at the triple line in the level $C = 0.5$. Note that the steady state solution is independent of fluid properties, such as viscosity and density ratios. Therefore, the solution applies to any set of fluid properties, so long as the surface wettability remains the same. Figure 2 shows the analytical and numerical value of the dimensionless height of the droplet, which can be calculated using the following equation [27]:

$$\frac{h}{R} = 2\sin\theta\sqrt{\frac{\pi}{2\theta - \sin 2\theta}}. \tag{41}$$

As we can see in Fig. 2, there is good agreement between the analytical and numerical results.

B. Contact angle on pillars

Because of the presence of pillars on the bottom surface, the apparent contact angle is greater than the equilibrium one in Eq. (40). The apparent contact angle is related to the state of the droplet on the pillars. If the droplet is in the Cassie state, the apparent contact angle can be calculated using the Cassie-Baxter equation [28]:

$$\cos\theta_a = -1 + \varphi_s(\cos\theta + 1), \tag{42}$$

where θ_a is the apparent contact angle due to the presence of pillars and φ_s is the solid fraction. Also, for a droplet in the Wenzel state, the Wenzel equation determines the value of θ_a [29],

$$\cos\theta_a = r\cos\theta, \tag{43}$$

where r is the ratio of the true surface area to the horizontal projection of the surface area. Numerical simulations are carried out for droplets in the Cassie and Wenzel states. The following parameters are set during simulations: $\rho_l = 1$, $\rho_g = 0.1$, $\tau_l = 0.5$, $\tau_g = 0.5$, $\sigma = 0.005$, $D = 4$, $\theta = 100^\circ$, $g = 4$ lu, $w = 4$ lu, and $h = 15$ lu.

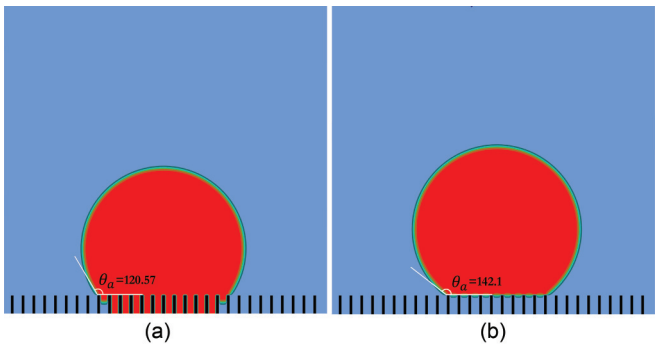

FIG. 3. Equilibrium shape of the droplet, (a) in Wenzel state and (b) in Cassie state.

Figure 3 shows the equilibrium state of the droplet. In Fig. 3(a), when the droplet is in the Wenzel state with $\theta = 100^\circ$, the numerical apparent contact angle is 120.57, and Eq. (43) predicts $\theta_a = 118.52^\circ$, which is consistent with the numerical value of θ_a. Also, when the droplet is in the Cassie state [Fig. 3(b)], the numerical apparent contact angle is 142.1°, and Eq. (42) predicts $\theta_a = 142.5^\circ$, which is consistent with the numerical value of θ_a, too.

C. Droplet evaporation

For validation of the droplet evaporation, numerical results are first compared to the D^2 law for the evaporation of a static droplet suspended in vapor. The D^2 law states that the area of the droplet during evaporation decreases linearly with time [30]:

$$D^{*2} = 1 - kt^*, \tag{44}$$

where $D^* = D/D_0$, $k = \frac{2\mu_l \dot{m}}{\pi\sigma D_0^2 \rho_l}$, and $t^* = \frac{2t\sigma}{\mu_l D_0}$. D_0 is the initial diameter, μ_l is the droplet viscosity, and $\dot{m}$ is the mass depletion rate due to evaporation which is calculated from the numerical results.

Figure 4 shows the results for a droplet with initial diameter $D_0 = 30$ lu, $\rho_l = 1$, $\rho_g = 0.1$, $\tau_l = 0.5$, $\tau_g = 0.5$, and $\sigma = 0.005$. It can be seen in Fig. 4 that the area of the droplet decreases linearly with time and has good agreement with the one predicted by Eq. (44).

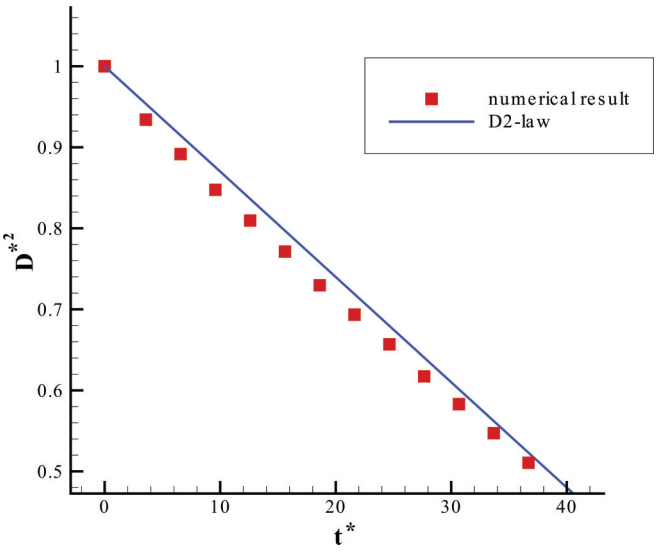

FIG. 4. Comparison of the numerical results with D^2 law.

IV. NUMERICAL RESULTS

In this section, pinning-depinning of the contact line due to the evaporation of the droplet in the presence of the pillars is investigated. Evaporation is modeled by the model of Safari *et al.* [25]. By applying the constant temperature T_g on the boundaries, the gas phase is held in this constant temperature, and it is assumed that the droplet remains in the saturation temperature T_s. Then, due to the temperature gradient and heat transfer at the interface, evaporation occurs. The Important dimensionless number that governs the evaporation of the droplet is the Stefan number, which is defined as the ratio of the sensible heat to the latent heat:

$$\mathrm{St} = \frac{C_p(T_g - T_{\mathrm{sat}})}{h_{fg}}. \tag{45}$$

h_{fg} and $(T_g - T_{\mathrm{sat}})$, are selected to realize a definite Stefan number. The following parameters are set during simulation: $T_g = 510$, $T_{\mathrm{sat}} = 500$, $\mathrm{St} = 0.4$, $\rho_l = 1$, $\rho_g = 0.1$, $\tau_l = 0.5$, $\tau_g = 0.5$, $\sigma = 0.005$, $D = 4$ lu, and $R = 40$ lu.

First, by measuring the value of the numerical apparent contact angle on different grid resolutions for the droplet in the Cassie state with $\theta = 100^\circ$ and $\varphi_s = 0.25$, the grid independency of the solution is tested. According to Eq. (42), θ_a should be 142.5°.

Table I shows the numerical value of θ_a on different grids. With doubling the grid from 200×220 to 400×440, θ_a does not change significantly. So, a 200×220 mesh is selected to carry out the simulations.

TABLE I. Numerical apparent contact angle on different meshes.

Mesh	Numerical apparent contact angle	Error
100×110	141.34°	0.8%
200×220	142.1°	0.28%
400×440	142.23°	0.18%

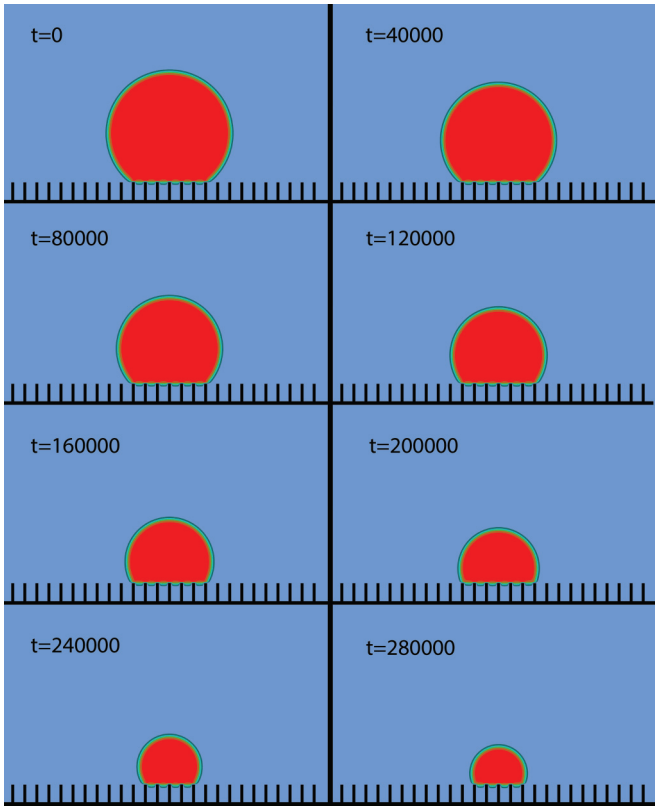

FIG. 5. Evaporation of the droplet on the pillars with $\theta = 100$, $\mathrm{St} = 0.4$ on a surface with $h = 15$ lu, $w = 4$ lu, and $g = 4$ lu.

A. Evaporation in the Cassie state

Figure 5 shows the contour of the phase composition during evaporation at different time steps. Evaporation starts when the contact line is pinned and after $t = 2\times10^5$, the contact line moves to the neighboring pillar.

Figure 6 shows the streamlines during evaporation in the Cassie state. The vapor from the interface moves upward and exits the domain from the open boundary.

1. Effect of contact angle

In Fig. 7(a), we can see that the evaporation starts in the CCR mode and for most of the droplet's lifetime, the droplet stays pinned at the initial pillar. In this case $\theta = 100^\circ$ and the apparent contact angle on the textured surface that is measured after the droplet is deposited on the surface is $\theta_a = 140.2^\circ$. This contact angle decreases continually until $t = 1.8\times10^5$. At this time when the contact angle reaches the receding contact angle, $\theta_r = 104.5^\circ$, the depinning force due to the unbalanced surface tension causes the droplet contact line to move. Due to this depinning force, the contact line moves to the next pillar until this depinning force is balanced with the pinning force of the pillar. This stick-slip pattern is continued until the end of the droplet lifetime. During this time, from the initial state until $t = 1.8\times10^5$, the contact radius is approximately constant (CCR mode). After that, until $t = 2.2\times10^5$, the contact radius decreases (due to the depinning effect). This situation, in which there is a variation in both contact angle

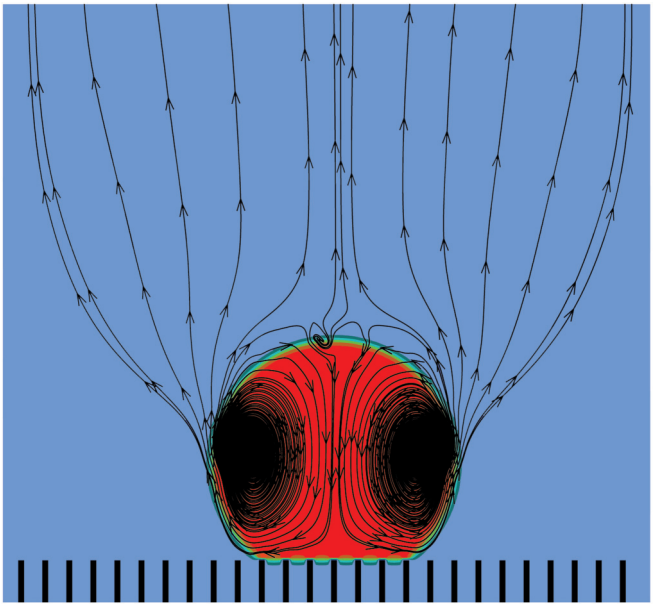

FIG. 6. Streamlines during evaporation of the droplet on the pillars with $\theta = 100$, St $= 0.4$ on a surface with $h = 15$ lu, $w = 4$ lu, and $g = 4$ lu.

and radius, is called the "mixed" mode. Figures 7(b)–7(e) show the phase field contour during CCR and the mixed mode. In (b), the droplet initially sits on the pillars with a contact angle of 140.2° and then the contact angle decreases in the CCR mode until (c), when $t = 1.8\times10^5$ goes into the mixed mode and depinning starts.

In the case of $\theta = 120°$ (Fig. 8), the apparent contact angle is $\theta_a = 153°$; this contact angle decreases in the CCR mode until $t = 1.7\times10^5$. After that until the time $t = 2.18\times10^5$, the mixed mode occurs and the contact radius decreases. When the contact angle reaches the receding state, $\theta_r = 127.5°$, at $t = 1.7\times10^5$, the depinning force is large enough to move the contact line forward and start the stick-slip pattern. Figures 8(b)–8(e) clearly show the pinning-depinning mechanisms for this droplet. In (b), the droplet with $\theta_a = 153°$ is sitting on top of the pillars. In (d) when 1.7×10^5, the droplet reaches the receding contact angle, $\theta_r = 127.5°$, and the mixed mode starts to occur and subsequently the contact line moves to the next pillar. In comparison to the case of $\theta = 100°$, the droplet has a greater receding contact angle and a smaller contact radius, and also depins slightly faster.

As mentioned above, pinning lasts until the contact angle reaches the receding contact angle. Then the unbalanced surface tension creates the driving force for the contact line movement. This out-of-balance surface tension force can be written as [31]

$$F_d = \sigma(\cos\theta_r - \cos\theta_a). \tag{46}$$

Figure 9 shows θ_r, θ_a, and F_D for three different values of θ. As we can see, by increasing the contact angle while keeping the solid fraction constant, θ_a becomes larger, which is the natural result of Eq. (42). On the other hand, θ_r also shows an increase in value. Furthermore, by increasing θ, the gap between θ_r and θ_a reduces and the depinning force decreases dramatically.

Figure 10 shows the nondimensional mass of the droplet versus time. The non-dimensional mass is defined as M/M_0 where M_0 is the initial mass before evaporation. As we can see in this figure, variation of mass against time is nonlinear and its slope decreases over time, which is consistent with the previously reported experimental results [20]. In the case of $\theta = 100°$, the droplet stays pinned at the initial location for approximately 50% of its lifetime. Results for $\theta = 120°$ are roughly the same.

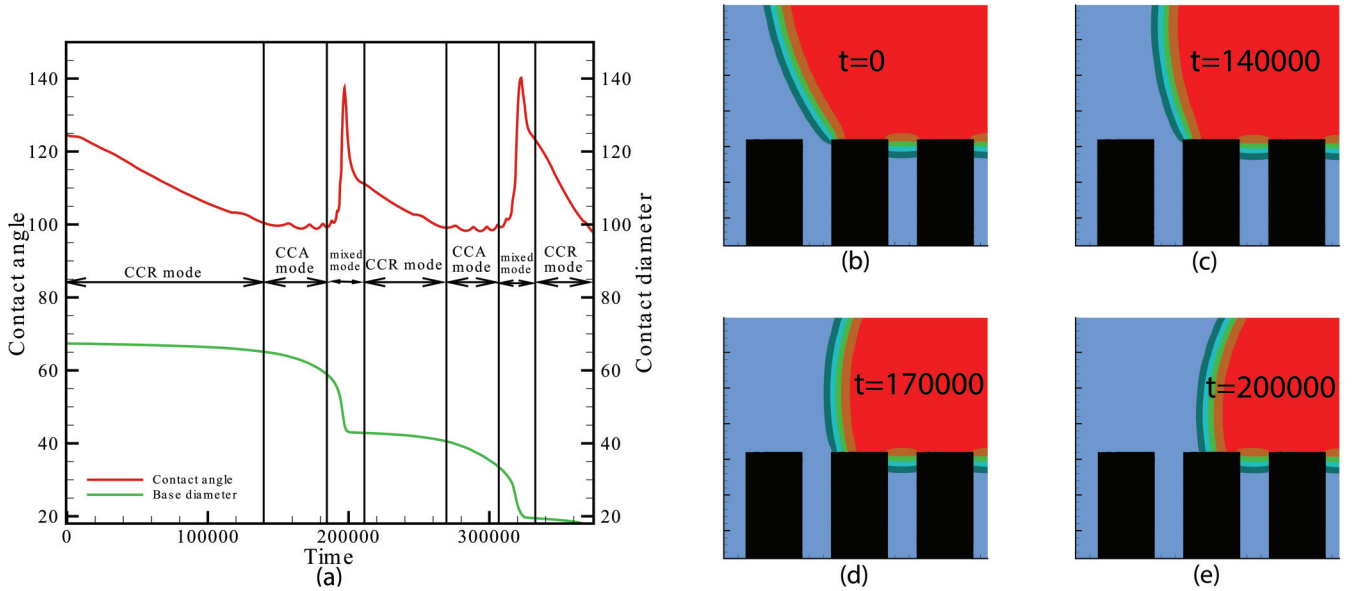

FIG. 7. Evaporation of the droplet initially in the Cassie state on substrate with $h = 15$ lu, $w = 4$ lu, $g = 4$ lu and $\theta = 100°$. (a) Variation of contact angle and contact radius. (b) Initial position of the droplet. Contact line is pinned on the pillar. (c) Evaporation causes change in contact angle, but contact line is still stuck to the pillar. (d) Slipping starts and depinning occurs. (e) Change in the contact line position is clear.

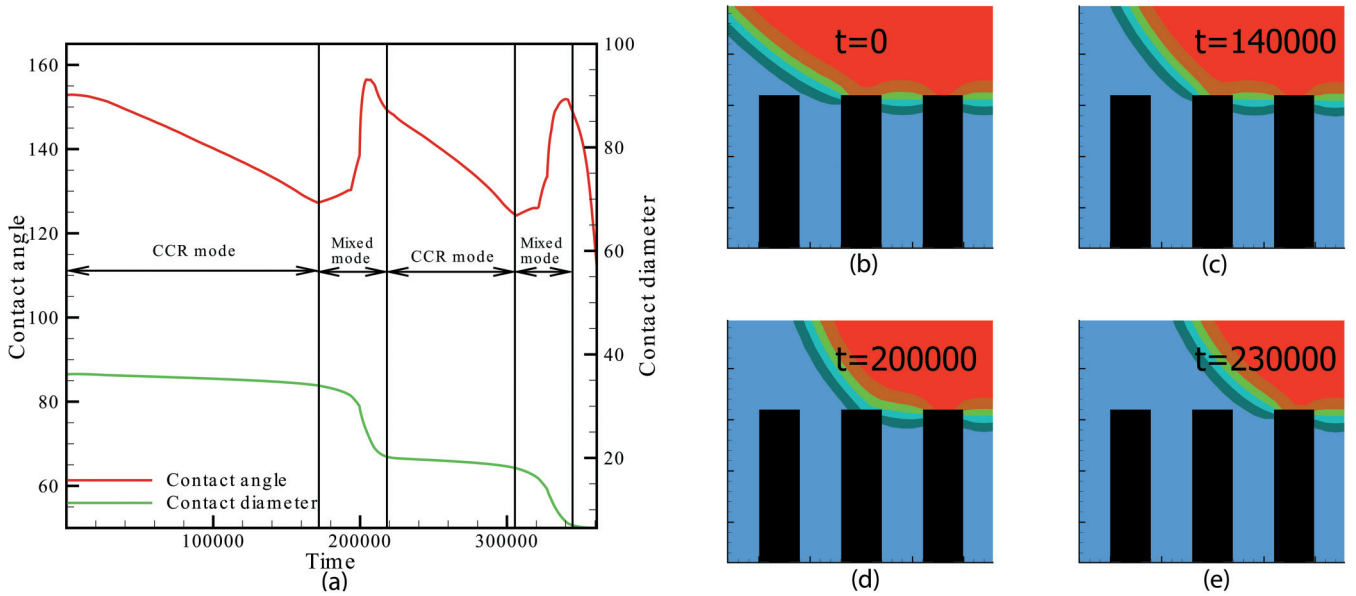

FIG. 8. Evaporation for the droplet initially in the Cassie state on substrate with $h = 15$ lu, $w = 4$ lu, $g = 4$ lu, and $\theta = 120°$.

2. *Effect of surface topology*

Figure 11 shows the variation of contact angle and contact radius with time for the droplet initially in the Cassie state on a substrate with $h = 15$ lu, $w = 8$ lu, $g = 4$ lu.

For $\theta = 100°$, by doubling the pillar width, the solid fraction increases, which according to Eq. (42) causes a decrease in θ_a. In this case $\theta_a = 125°$, which is 18° smaller than the surface with $w = 4$ lu. Also, the receding contact angle changes slightly with increasing the solid fraction. As we can see in Fig. 11(a), evaporation starts in the CCR mode. Subsequently, the CCA mode takes place, in which the contact angle is approximately constant. Then, a transition to the mixed mode, followed by variations in both the contact angle and radius, is observed. In fact, generally there is a CCA mode period after the initial CCR mode period during droplet evaporation on the textured surface. However, from the numerical simulation standpoint, there is an inherent limitation due to the application of the diffuse interface model. To accurately simulate the problem, the interface thickness needs to be as small as possible compared to the smallest length scale of the problem. The smallest length scale in our problem is the pillar width w. In the case of $w = 4$ lu, $\frac{D}{w} = 1$, as we can see in the previous section, after the CCR mode, the droplet goes into the mixed mode, and the CCA mode is not captured on this surface. However, in the surface with $w = 8$ lu, $\frac{D}{w} = 0.5$, a nearly constant contact angle exists between the CCR and the mixed modes.

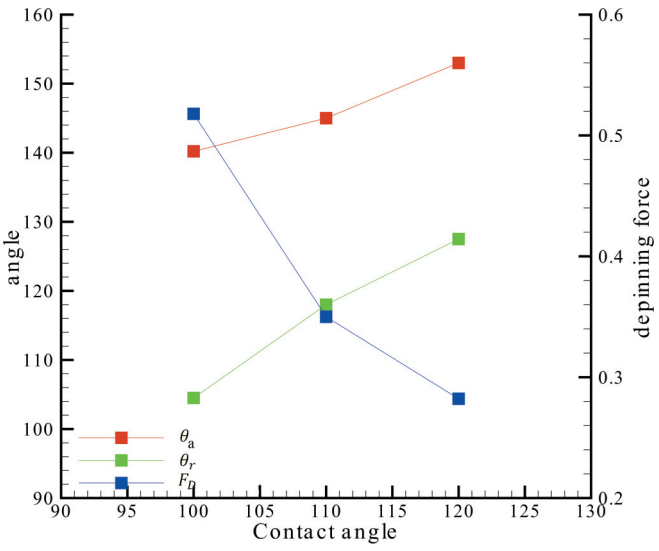

FIG. 9. Variation in θ_r, θ_a, and F_D with contact angle.

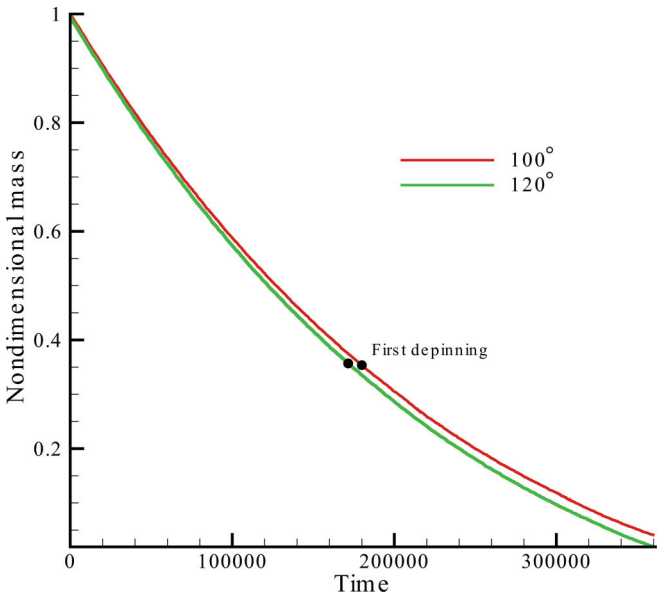

FIG. 10. Nondimensional mass versus time in two different contact angles.

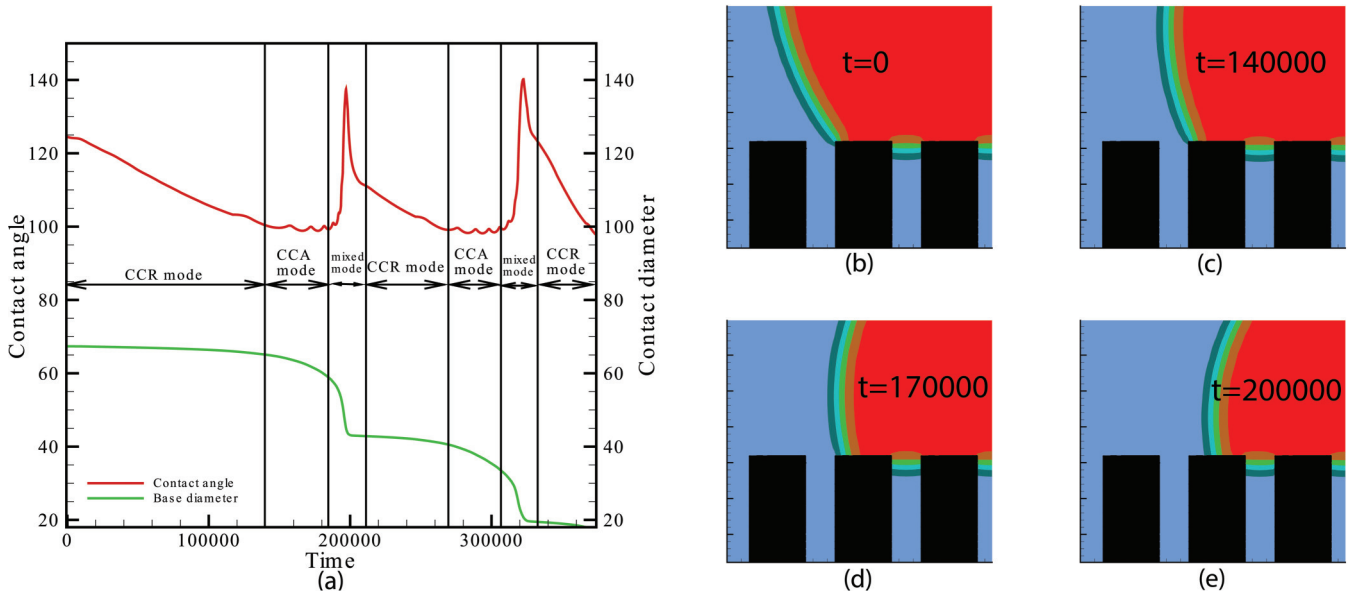

FIG. 11. Evaporation for the droplet initially in the Cassie state on substrate with $h = 15$ lu, $w = 8$ lu, $g = 4$ lu, and $\theta = 100°$. (a) Variation of contact angle and contact radius. (b) Initial position of the droplet. Contact line is pinned on pillar. (c) Slipping starts and depinning occurs. Droplet goes to the CCA mode. (d) Droplet slips on the pillar in CCA mode.

As we can see in Fig. 12, by increasing the pillar width, the quasiequilibrium contact angle of the droplet decreases nonlinearly, but the receding contact angle is approximately constant. Decreasing θ_r causes a decrease in the depinning force. Then, on a surface with larger pillar width, the droplet needs a smaller depinning force. These results are consistent with the reported experimental results in [13,15].

B. Evaporation in the Wenzel state

Figure 13 shows the streamlines during evaporation in the Wenzel. Like the Cassie state, vapor from the interface moves upward and exits the domain from the open boundary.

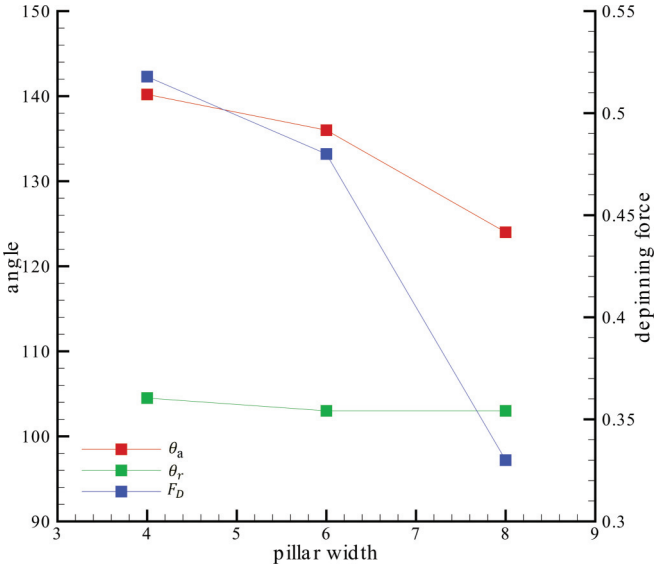

FIG. 12. Variation in θ_r, θ_a, and F_D with pillar width.

Figure 14 shows the evaporation in the Wenzel state on a surface with $\theta = 120°$. The apparent contact angle is 129°. When evaporation takes place, the contact angle starts to decrease slowly over time. From the initial moment of the evaporation, until $t = 1.9\times10^5$, the contact line moves on the top of the pillar and then becomes pinned in the corner. Subsequently, the contact radius remains constant and the contact angle starts to decrease faster. This decrease in contact angle is continued until the end of the droplet lifetime.

Figure 15 shows the evaporation on a surface with $\theta = 100°$. On this surface, with $h = 15$ lu, $w = 4$ lu, $g = 4$ lu,

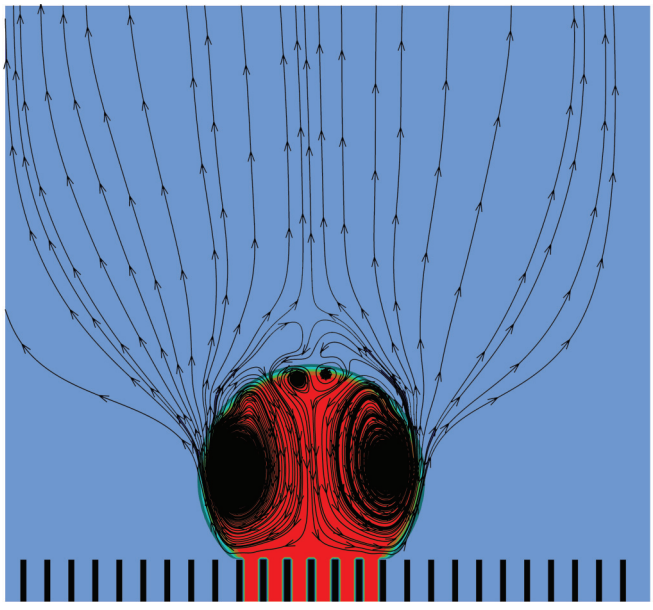

FIG. 13. Streamlines during evaporation of the droplet in the Wenzel state, with $\theta = 120$, St $= 0.4$ on a surface with $h = 15$ lu, $w = 4$ lu, and $g = 4$ lu.

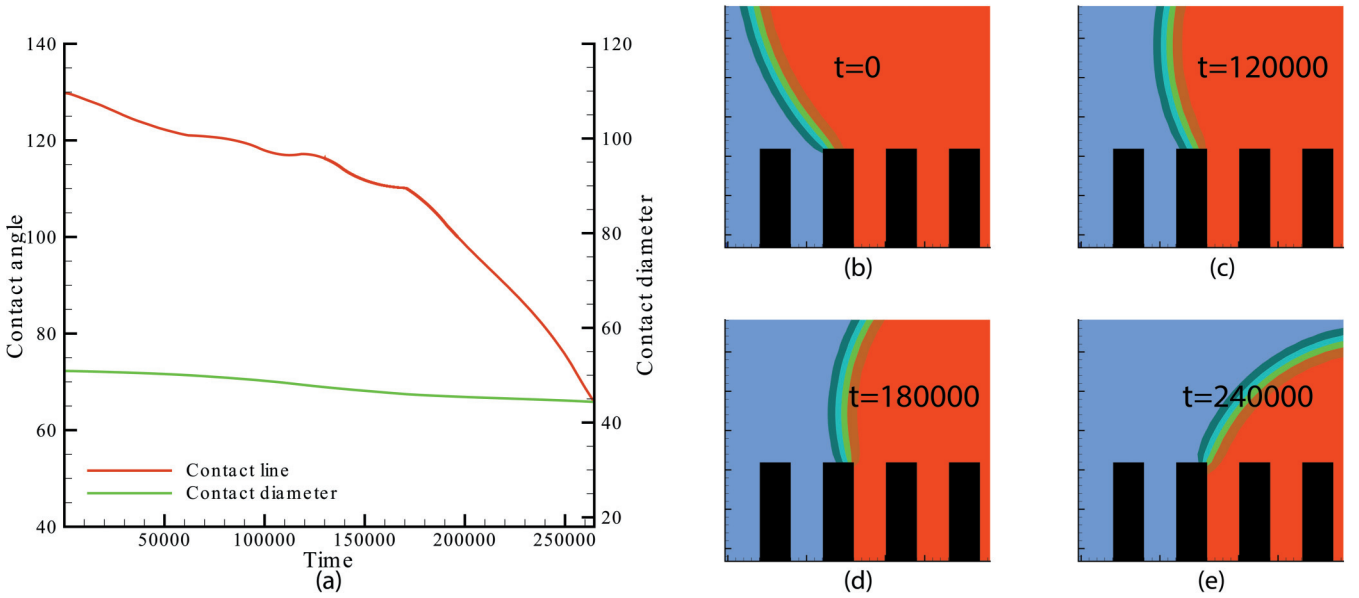

FIG. 14. Evaporation for the droplet initially in the Wenzel state on substrate with $h = 15$ lu, $w = 4$ lu, $g = 4$ lu, and $\theta = 120^\circ$. (a) Variation of contact angle and contact radius. (b) Initial position of the droplet. Contact line is pinned on pillar. (c) Contact line slips very slightly toward the inner corner of the pillar. (d) Droplet slips on the pillar. (e) Contact line is stuck and contact angle decreases over time.

the apparent contact angle is 117°. Behavior of the contact line during evaporation is nearly the same as the surface with $\theta = 120^\circ$.

V. CONCLUSION

In this work, we studied the pinning-depinning mechanisms of a liquid droplet during evaporation on a patterned surface using the lattice Boltzmann method. When the droplet was initially in the Cassie state, the stick-slip behavior of the contact line was observed on the surfaces with different pillar widths and different equilibrium contact angles. The results obtained from the numerical simulations on the patterned surface demonstrated that the receding contact angle increases by increasing the equilibrium contact angle, but does not change significantly by increasing the pillar width. Also, the depinning force per unit length decreases dramatically by increasing the pillar width or contact angle, but during evaporation, the CCA mode is not accurately captured. The reason is most likely due to the diffuse interface model. For handling this problem, the interface thickness needs to be as small as possible compared to the pillar width. For evaporation in the Wenzel state, it is observed that the contact line remains approximately in its initial location for the entirety of the droplet lifetime and the contact angle decreases over time. The

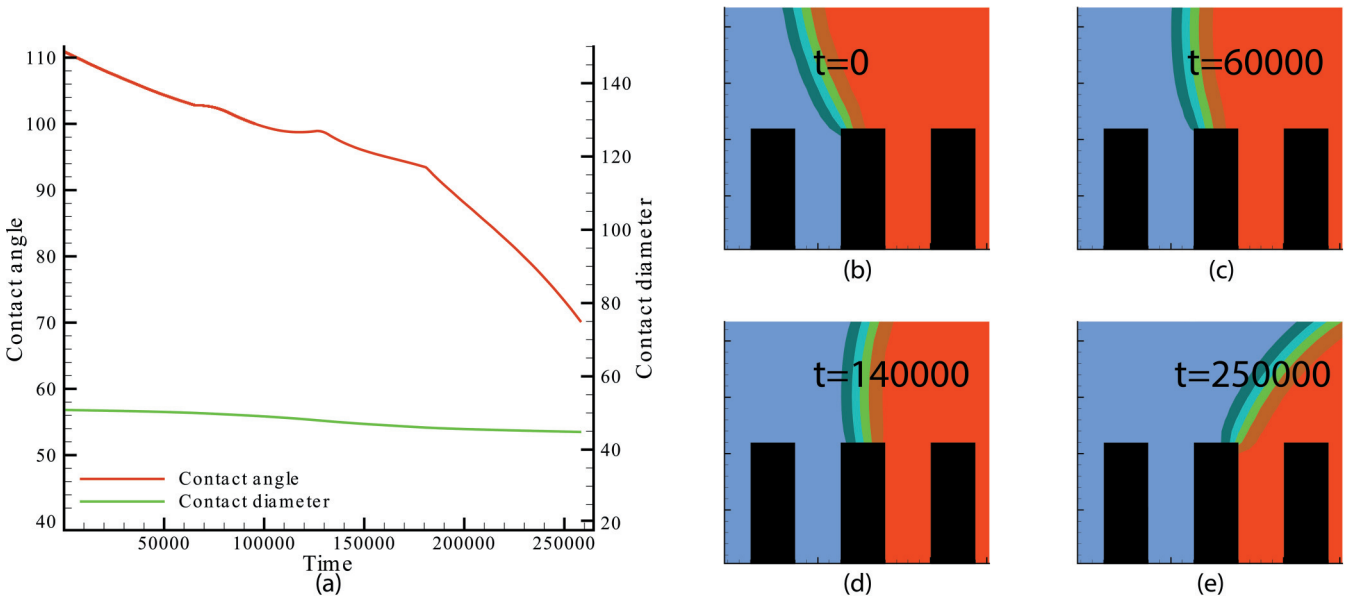

FIG. 15. Evaporation for the droplet initially in the Wenzel state on substrate with $h = 15$ lu, $w = 4$ lu, $g = 4$ lu, and $\theta = 100^\circ$.

current two-dimensional model is not capable of modeling the Cassie-Wenzel transition and extending the model to three dimensions could be an interesting topic for further future studies.

[1] Q. Li, Y. T. Zhu, I. A. Kinloch, and A. H. Windle, J. Phys. Chem. B **110**, 13926 (2006).
[2] A. Ebrahimi, P. Dak, E. Salm, S. Dash, S. V. Garimella, R. Bashir, and M. A. Alam, Lab Chip **13**, 4248 (2013).
[3] P. Calvert, Chem. Mater. **13**, 3299 (2001).
[4] J. Jing *et al.*, Proc. Natl. Acad. Sci. USA **95**, 8046 (1998).
[5] S. T. Chang and O. D. Velev, Langmuir **22**, 1459 (2006).
[6] G. McHale, S. Aqil, N. Shirtcliffe, M. Newton, and H. Y. Erbil, Langmuir **21**, 11053 (2005).
[7] K. Birdi and D. Vu, J. Adhes. Sci. Technol. **7**, 485 (1993).
[8] S. Kulinich and M. Farzaneh, Appl. Surf. Sci. **255**, 4056 (2009).
[9] N. Anantharaju, M. Panchagnula, and S. Neti, J. Colloid Interface Sci. **337**, 176 (2009).
[10] J. Bico, U. Thiele, and D. Quéré, Colloids Surf. A **206**, 41 (2002).
[11] R. Picknett and R. Bexon, J. Colloid Interface Sci. **61**, 336 (1977).
[12] J. M. Stauber, S. K. Wilson, B. R. Duffy, and K. Sefiane, J. Fluid Mech. **744**, R2 (2014).
[13] X. Chen, R. Ma, J. Li, C. Hao, W. Guo, B. L. Luk, S. C. Li, S. Yao, and Z. Wang, Phys. Rev. Lett. **109**, 116101 (2012).
[14] S. Dash and S. V. Garimella, Phys. Rev. E **89**, 042402 (2014).
[15] W. Xu and C.-H. Choi, Phys. Rev. Lett. **109**, 024504 (2012).
[16] C.-H. Choi and C.-J. C. Kim, Langmuir **25**, 7561 (2009).
[17] Y. O. Popov, Phys. Rev. E **71**, 036313 (2005).
[18] X. Zhang, S. Tan, N. Zhao, X. Guo, X. Zhang, Y. Zhang, and J. Xu, ChemPhysChem. **7**, 2067 (2006).
[19] H. Gelderblom, A. G. Marin, H. Nair, A. van Houselt, L. Lefferts, J. H. Snoeijer, and D. Lohse, Phys. Rev. E **83**, 026306 (2011).
[20] S. Dash and S. V. Garimella, Langmuir **29**, 10785 (2013).
[21] B. Sobac and D. Brutin, Langmuir **27**, 14999 (2011).
[22] B. Sobac and D. Brutin, Phys. Rev. E **86**, 021602 (2012).
[23] T. Inamuro, T. Ogata, S. Tajima, and N. Konishi, J. Comput. Phys. **198**, 628 (2004).
[24] T. Lee and P. F. Fischer, Phys. Rev. E **74**, 046709 (2006).
[25] H. Safari, M. H. Rahimian, and M. Krafczyk, Phys. Rev. E **88**, 013304 (2013).
[26] K. Connington and T. Lee, J. Comput. Phys. **250**, 601 (2013).
[27] P.-G. De Gennes, F. Brochard-Wyart, and D. Quéré, *Capillarity and Wetting Phenomena: Drops, Bubbles, Pearls, Waves* (Springer Science & Business Media, Berlin, 2013).
[28] A. Cassie and S. Baxter, Trans. Faraday Soc. **40**, 546 (1944).
[29] R. N. Wenzel, Ind. Eng. Chem. **28**, 988 (1936).
[30] A. Mazloomi Moqaddam, D. Derome, and J. Carmeliet, Langmuir **34**, 5635 (2018).
[31] K. Sefiane, J. Colloid Interface Sci. **272**, 411 (2004).